Global characterization of Rossby waves at several spectral bands

Paulo S. Polito
Instituto Nacional de Pesquisas Espaciais, São José dos Campos, São Paulo, Brazil

W. Timothy Liu
Jet Propulsion Laboratory, California Institute of Technology, Pasadena, California, USA

Received 23 August 2000; revised 13 November 2001; accepted 7 December 2001; published 31 January 2003.

[1] Global sea surface height anomaly signals from the TOPEX/Poseidon satellite altimeter from 1992 to 2000 are filtered into several spectral bands. These bands include propagating (Rossby, Kelvin, and tropical instability waves) and nonpropagating (annual and interannual basin-scale variability and eddies) signals. These signals are decomposed through a series of finite impulse response band-pass filters. Phase speed, period, wavelength, and amplitude are estimated. Signal-to-noise ratio, methodological errors, and natural variability are also estimated. Results are shown for the Pacific, Atlantic, and Indian basins for four Rossby wave components with periods between 3 and 24 months. Equatorial Kelvin waves and tropical instability waves are shown as peripheral results. The clearest and most energetic wave signals are generally observed for annual Rossby waves. Semiannual Rossby waves often have the largest amplitudes near the tropics. The Rossby wave phase speeds are in agreement with the linear theory, except for a ~25% bias toward high speeds found in mid to high latitudes. This revitalizes the idea that on the average the Rossby wave signal in the ocean is in the form of free waves. *INDEX TERMS:* 4508 Oceanography: Physical: Coriolis effects; 4556 Oceanography: Physical: Sea level variations; 4275 Oceanography: General: Remote sensing and electromagnetic processes (0689); *KEYWORDS:* Rossby waves, tropical instability waves, FIR filters, Kelvin waves, phase speed

Citation: Polito, P. S., and W. T. Liu, Global characterization of Rossby waves at several spectral bands, *J. Geophys. Res.*, *108*(C1), 3018, doi:10.1029/2000JC000607, 2003.

1. Introduction

[2] Rossby waves are a solution for the problem of adjustment of the geophysical fluid to large scale perturbations. This solution is based on the conservation of angular momentum, or more specifically potential vorticity (hereafter PV), and proved to be key to understand the large scale oceanic and atmospheric circulation. The basic theory together with a historical perspective on the evolution of these ideas is now part of the standard literature on geophysical fluid dynamics [e.g., *Gill*, 1982; *Pedlosky*, 1986]. The initial theory [*Rossby*, 1938] has been extended to a great variety of cases [e.g., *White*, 1977; *Lippert and Käse*, 1985; *Herrmann and Krauß*, 1989] and tested with a number of in situ [e.g., *Kessler*, 1989; *White and Saur*, 1981; *White*, 1985] and satellite [e.g., *Chelton and Schlax*, 1996; *Polito and Cornillon*, 1997; *Cipollini et al.*, 1997] observations and numerical simulations [e.g., *Killworth et al.*, 1997; *Qiu et al.*, 1997; *Wang et al.*, 1998; *White et al.*, 1998].

[3] This study focuses on the global characterization of long, first mode baroclinic Rossby waves. The basic assumptions are that the wavelength is significantly longer than the Rossby radius of deformation, and as a first approximation the ocean behaves as a two-layer system with the vertical displacement of the interface induced by the waves. The linear theory indicates that the long waves are nondispersive and transport potential energy westward that helps to maintain the mid latitude gyres and to intensify the western boundary currents.

[4] TOPEX/Poseidon (T/P) provided for the first time a multi-year global time series of accurate measurements of sea surface height anomaly (η). The sea surface height changes either due to a net flux of mass or variations in the depth-averaged density of the water column. The latter which has a relatively longer temporal scale can be caused by any perturbation in the density field such as the passage of a baroclinic Rossby wave. In a two-layer ocean model the vertical displacement of the interface (thermocline) implies that the total amount of heat stored locally in the water column changes with the passage of the waves. There is a direct correspondence between potential energy, sea surface height anomaly and heat storage [*Chambers et al.*, 1997; *Polito et al.*, 2000].

[5] *Chelton and Schlax* [1996] (hereafter CS) proposed that the observed phase speed of Rossby waves (c_p) in mid to high latitudes were faster than the linear theory by a factor of two. Their estimates of c_p were based on "stacking" zonal-temporal diagrams of η. *Zang and Wunch* [1999] (hereafter ZW) proposed a different approach in which the phase speeds are estimated from high-resolution zonal frequency-wave number spectral analysis applied to multiple

0148-0227/03/2000JC000607$09.00

narrow bands. ZW showed that a significant part of the propagating signals in seven locations in the North Pacific have c_p estimates consistent with the linear theory. That prompted for a review of the conclusions of CS. Furthermore, ZW presented c_p estimates that do not decay with frequency as fast as the linear theory predicts. One of the objectives of this study is to estimate c_p and other parameters of Rossby waves at several regions of the zonal wave number-frequency spectrum and compare the results with both CS and ZW.

[6] This study uses a series of finite impulse response (FIR) filters to separate (1) propagating from nonpropagating signals, (2) westward from the eastward propagating signals and (3) several components of westward propagating signals. The latter are identified as Rossby (or planetary) waves and their c_p, period T, wavelength L, fractional variance V, amplitude A, and signal-to-noise ratio S/N are estimated for every component and degree of latitude. The same technique has been successfully applied to compare heat storage from T/P and in situ data by *Polito et al.* [2000] since the effect of salinity on η is small [*Sato et al.*, 1999a]. A modified Radon transform technique [*Polito and Cornillon*, 1997; *Cipollini et al.*, 1997] was used to estimate c_p. This method is similar to that used by CS. Error estimates are presented as well as estimates of the natural variability.

[7] A brief summary of the theory is presented in the next section. Section 3 reviews the methodology and addresses the standard T/P data treatment, the main aspects of the FIR filter, the estimation of wave parameters, their associated measurement errors and variability. Technical details of the data treatment are in appendix A. In section 4 the main results are presented and discussed. These results are organized to illustrate the performance of the filters, present the latitudinal distribution of wave parameters and their average errors and address the spatial distribution of the wave signals. Section 5 has the conclusions.

2. Theory

[8] The focus of this study is on long baroclinic Rossby waves. These waves are the basic ocean response to large-scale perturbations in the depth of the pycnocline. Pycnocline depth variations can be interpreted as stretching and compression of the water column and therefore as variations in the PV field. These variations are considered in relation to a background PV gradient imposed by planetary vorticity β, the meridional gradient of the Coriolis parameter f. Oscillations occur when a water parcel is perturbed from its basic PV state (f/H, where H is the layer thickness). PV conservation acts as a restoring agent and ensures oscillation around the initial state.

[9] The assumption of a linear, flat bottom, mid latitude, shallow water ocean in which PV is conserved leads to the dispersion relation

$$\omega = \frac{-\beta k}{k^2 + l^2 + R_1^{-2}}, \tag{1}$$

where ω is the frequency, k the zonal and l the meridional wave numbers, and R_1 is the Rossby radius of deformation for the first baroclinic mode; $R_1 = c_1/f$ where c_1 is the internal gravity wave phase speed for the first vertical mode. If the propagation is zonal, the phase speed is given by $c_p = \omega/k$ and the group speed by $c_g = \frac{\partial \omega}{\partial k}$. The c_g is the speed at which the wave energy propagates and becomes zero when $\omega = -\frac{1}{2}\frac{\beta}{R_1}$. This introduces a critical latitude, poleward of which there is no wave propagation.

[10] Only the zonal propagation is addressed in this study because meridional Rossby wave propagation patterns are significantly less persistent than their zonal counterparts [*Polito and Cornillon*, 1997]. As a consequence, the errors associated with meridional phase speed estimates are relatively large. In addition, the methodology described in section 3 cannot be applied to the meridional-temporal data because the meridional phase speed varies significantly (changes sign) along the same longitude.

[11] If the propagation is mainly zonal and the waves are long, $k \ll 1/R_1$, equation (1) simplifies to

$$\omega = -\beta k R_1^2 \tag{2}$$

[12] From equation (2), $c_p = \omega/k = -\beta R_1^2$. Therefore, c_p has a strong dependence on the latitude ϕ through β and f. $c_p \propto \frac{\cos(\phi)}{\sin(\phi)^2}$ means that a poleward decrease in magnitude is relatively fast at low latitudes and slow at high latitudes.

[13] In the equatorial regions f is evanescent and the theory is adapted through the use of an equatorial β-plane approximation[*Gill*,1982].Thisresultsinc_{pm}=$-c_n/(2m+1)$ for long baroclinic Rossby waves, where c_n is the phase speed for baroclinic mode n and m is the meridional mode.

[14] All the results above come from first order approximations. In reality, bottom topography, mean geostrophic currents, and any other large scale effects that change the background PV gradient will affect the dispersion relation just as β does. This consideration leads to an effective β field [*Herrmann and Krauß*, 1989] that is no longer constant at each latitude and its implication to meridional propagation is ignored in equation (2). In addition, the pycnocline displacement due to the wave also affects R_1 and leads to a nonlinear correction of the theory. A last observation is that equation (2) does not take into account atmospheric forcing, an important aspect of the dynamics in focus [*White*, 1985; *Polito*, 1997; *Wang et al.*, 1998].

3. Methods

[15] The sea surface height estimates are obtained from the T/P altimeter data record distributed by the Jet Propulsion Laboratory Physical Oceanography Distributed Active Archive Center published for the World Ocean Circulation Experiment conference. The η data are calculated in relation to a 8-year average (1993–2000) and presented in bin-averaged grid maps of $0.5^\circ \times 0.5^\circ \times 10$ days. The data cover latitudes between 66°S and 66°N, and from October 1992 to December 2000. All standard corrections are applied [*Benada*, 1997].

[16] The bin-averaged data are bicubically interpolated to a $1^\circ \times 1^\circ$ grid, a spatially continuous data set required by the filter algorithm. Maps of the sea surface height anomaly as a function of longitude and latitude, $\eta_o(x, y)$, for the Pacific, Atlantic, and Indian basins are converted to zonal-temporal diagrams of $\eta_o(x, t)$, one for every degree of

latitude. Shallow areas ($H \leq 1000$ m) and zonally enclosed water bodies are excluded to avoid border problems related to limitations inherent to the altimeter data and to the filter. Small islands ($x \leq 3°$) are ignored, only continuous open-ocean areas ($x > 20°$) are used.

[17] The η_o is decomposed through FIR filters into:

$$\eta_o = \eta_t + \eta_{24} + \eta_{12} + \eta_6 + \eta_3 + \eta_1 + \eta_K + \eta_E + \eta_r. \quad (3)$$

[18] η_t is the nonpropagating, basin-scale signal. It includes thermal signals advected by currents and variability due to air-sea heat exchange with seasonal and interannual periodicity such as ENSO. η_t is obtained through the application of symmetric Gaussian filters insensitive to propagation that capture temporal scales of one year or more and wavelengths similar to the local basin width. η_{24} to η_3 are the westward propagating Rossby waves with approximate periods of 24, 12, 6, and 3 months. η_1 has a period of 1.5 months and is dominated by tropical instability waves (TIWs) [*Polito et al.*, 2001; *Liu et al.*, 2000]. η_K is present only in the equatorial region (Table 2) as a fast eastward propagating signal identified as equatorial Kelvin waves. The η_K signal is not as clear in the original data as the Rossby wave signal. Therefore, it is not resolved in multiple frequency bands. Instead, a single filter with a central period of 2 months is applied. This filter distinguishes eastward propagating Kelvin from Yanai waves because the period of the latter is approximately 15 days. η_E is obtained after the large-scale and propagating components are subtracted from the original data. A symmetric Gaussian FIR filter centered at 50 days and 5° is applied to obtain what we called "mesoscale eddy field" for lack of a better term. This filter is not sensitive to propagation. Therefore, if an eddy does not propagate with the local Rossby wave phase speed, it will be included in this component. η_r is the residual dominated by small scale or high frequency signals and instrument noise. η_E and η_r also include barotropic signals [*Tierney et al.*, 2000; *Stammer et al.*, 2000] that are outside the scope of this study.

[19] The η_{24}, η_{12}, η_6, and η_3 components of equation (3) are used to identify the presence and characteristics of Rossby waves based on statistical parameters. The characterization of these signals as Rossby waves takes into account that they propagate westward with a c_p within a factor of two of theoretical predictions and that their wavelength is long compared to the local Rossby radius of deformation. The statistical significance of these signals is measured by the parameters A, V, and S/N associated with each component. If no significant wave signal is present at a given spectral band the filtered signal will have low amplitude, explain little or nothing of the total variance, and have a low signal-to-noise ratio. A graphical example of the filter performance is shown in the Figure 8. Further validation of equation (3) is presented by *Polito et al.* [2000] where the sum of the filtered altimeter signals is converted to heat content. The satellite based heat content is strongly correlated to in situ estimates in several areas of the global oceans. The heat content correlation shows the correspondence between the sea surface height anomaly and the vertical displacement of the main thermocline, a characteristic of the first mode baroclinic waves.

[20] ZW states that "A rigorous determination of phase velocity in a broadband situation requires isolating narrowband frequencies and wave numbers so as to, among other things, clearly distinguish the phase and group velocities in longitude-time diagrams.." The method used in this study is in partial agreement with this statement because c_p is estimated for several frequency bands. The definition of narrowband is subjective. The wave components defined in equation (3) have a finite spectral width and are centered at the indicated periods. The width of the bands is such that there are no gaps between one band and its neighbors. Consecutive bands overlap because the filter decay between each pass and stopband is not abrupt. Therefore, in the context of this study the term annual Rossby wave means a periodic anomaly contained in the η_{12} band with a dominant period is between approximately 9 and 18 months. A practical consequence of this definition of bands is that, for example, a wave with a period of 140 days can either be in the η_6 or η_3 bands (but not in both).

[21] The filtered data are obtained at each degree of latitude as a function of longitude and time. These data are subdivided into blocks that measure approximately T by L and the wave parameters c_p, T, L, A, V and S/N are estimated within each data block. These parameters are therefore a function of longitude and time within each latitude. Figure 1 shows an example of the estimated zonal phase speed for 28.5°N in the Pacific. The top plot shows the mean distribution in space and the bottom plot the distribution in time. There are significant variations of c_p in time and space, with c_p slightly faster in the western half of the basin where the thermocline deepens. The c_p estimates plotted in Figure 1 were obtained from the same data illustrated in Figure 2. The mean values for all latitudes and basins are shown in Figures 3, 4, and 5 (the c_p for η_K is multiplied by -1; A, V and S/N were smoothed to improve readability). The overall mean of the measurement error (ME) and standard deviation (SD) are presented in Table 1.

[22] The simplest way to estimate c_p is to find the slope of the patterns of propagation in zonal-temporal diagrams. This process is automatized with a procedure based on the Radon transform. In essence, this method rotates the coordinate system of the zonal-temporal diagrams until the patterns are aligned with the vertical axis. This alignment is optimal when the variability projected onto the horizontal axis is maximized. The c_p is the tangent of the angle of rotation that maximizes the projected variability. Estimates of T, L, and A are based on least-square fit of sinusoidal functions. Details of the parameter and error estimation are described in Appendix A.

4. Results

4.1. General Aspect of the Filtered T/P Data

[23] The performance of both the filter and the c_p estimation method is illustrated in Figure 2 for 28.5°N in the Pacific. The η_s is the sum of the filtered components such that $\eta_o = \eta_s + \eta_r$. Not all components of equation (3) are shown because of the latitudinal limitation imposed by the resolution of T/P (Table 2).

[24] A comparison between η_o and η_s (or η_r) indicates that the filter does not change the overall characteristics of the data as the residual η_r has no propagation patterns.

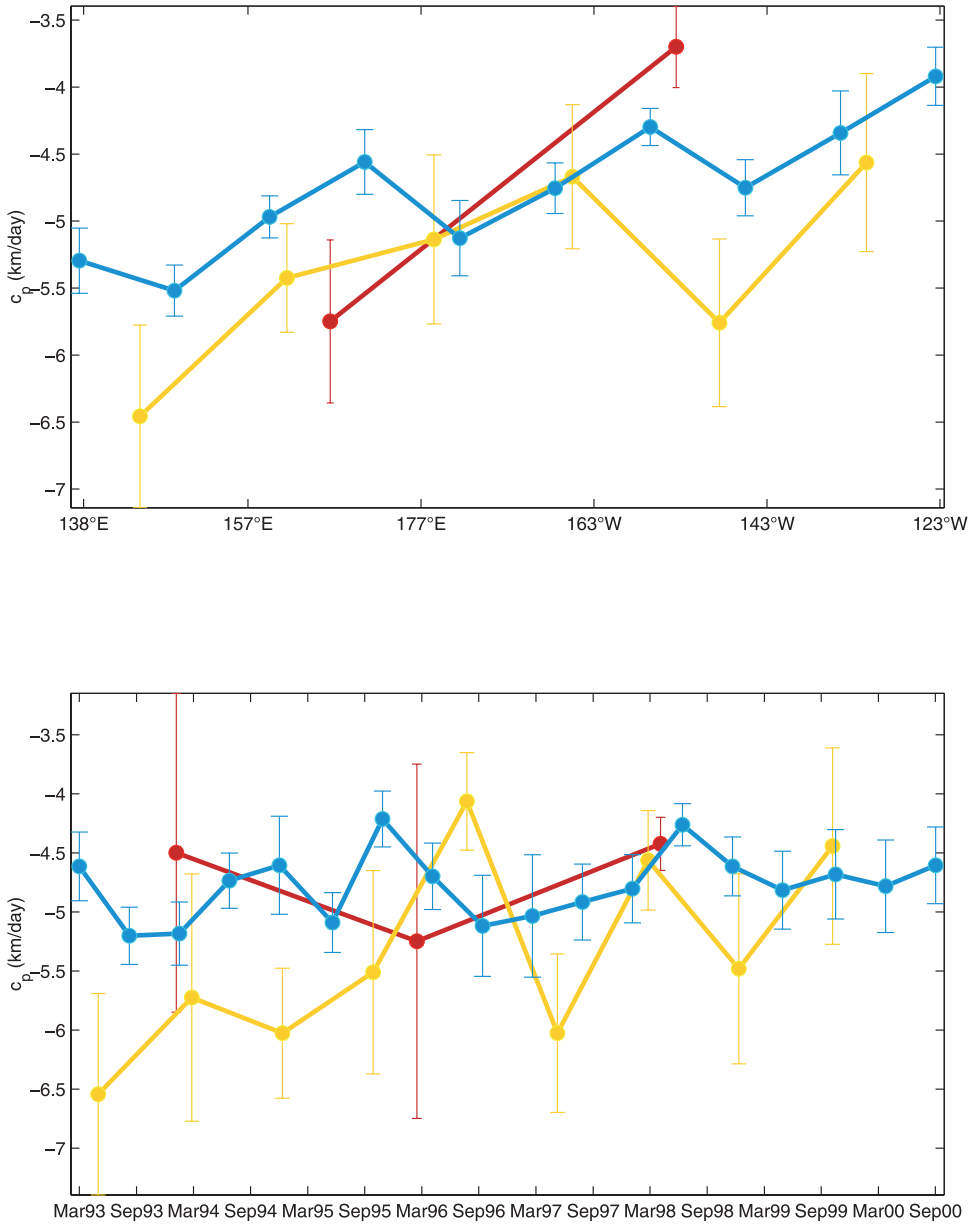

Figure 1. Zonal (top) and temporal (bottom) distribution of c_p estimates at 28.5°N in the Pacific. The blue, yellow, and red lines correspond to estimates based on η_6, η_{12}, and η_{24}, respectively. The error bars represent the standard error of the mean.

More specifically, it does not change the phase or propagation speed of the meso to large-scale signals. The fidelity of the filtered data has been confirmed through comparisons with hydrographic data [*Polito et al.*, 2000] in terms of oceanic heat storage. In addition to the propagating signals there is a significant fraction of the variance associated with the basin-scale, mostly seasonal (η_t), and meso-scale eddy (η_E) fields. A detailed characterization of these components would be too long for this study.

[25] At 28.5°N in the Pacific (Figure 2) Rossby waves comprise on average 38% of the variance of the interpolated T/P data product η_o. The η_6 alone explains 21% of the total variance while η_{12} and η_{24} explain 9% and 8%, respectively. Most of the Rossby wave energy is found in the western half of the basin. Dash-dot diagonal lines correspond to the average c_p of −4.3(±0.9) km/day for η_{24} − 5.2(±1.4) km/day for η_{12} − 4.5(±0.9) km/day for η_6. The overall alignment between the wave fronts and the phase lines is a direct validation of the estimated phase speed. The alignment is better in the western basin because the waves are stronger and more regular there. Furthermore, the average excludes low amplitude regions. This particular latitude in the Pacific was chosen because it has clear Rossby wave signals and c_p can be compared with previous studies.

4.2. The Mean Wave Parameters

[26] A comprehensive analysis of all parameters estimated in this study would be too long: six parameters (*C*,

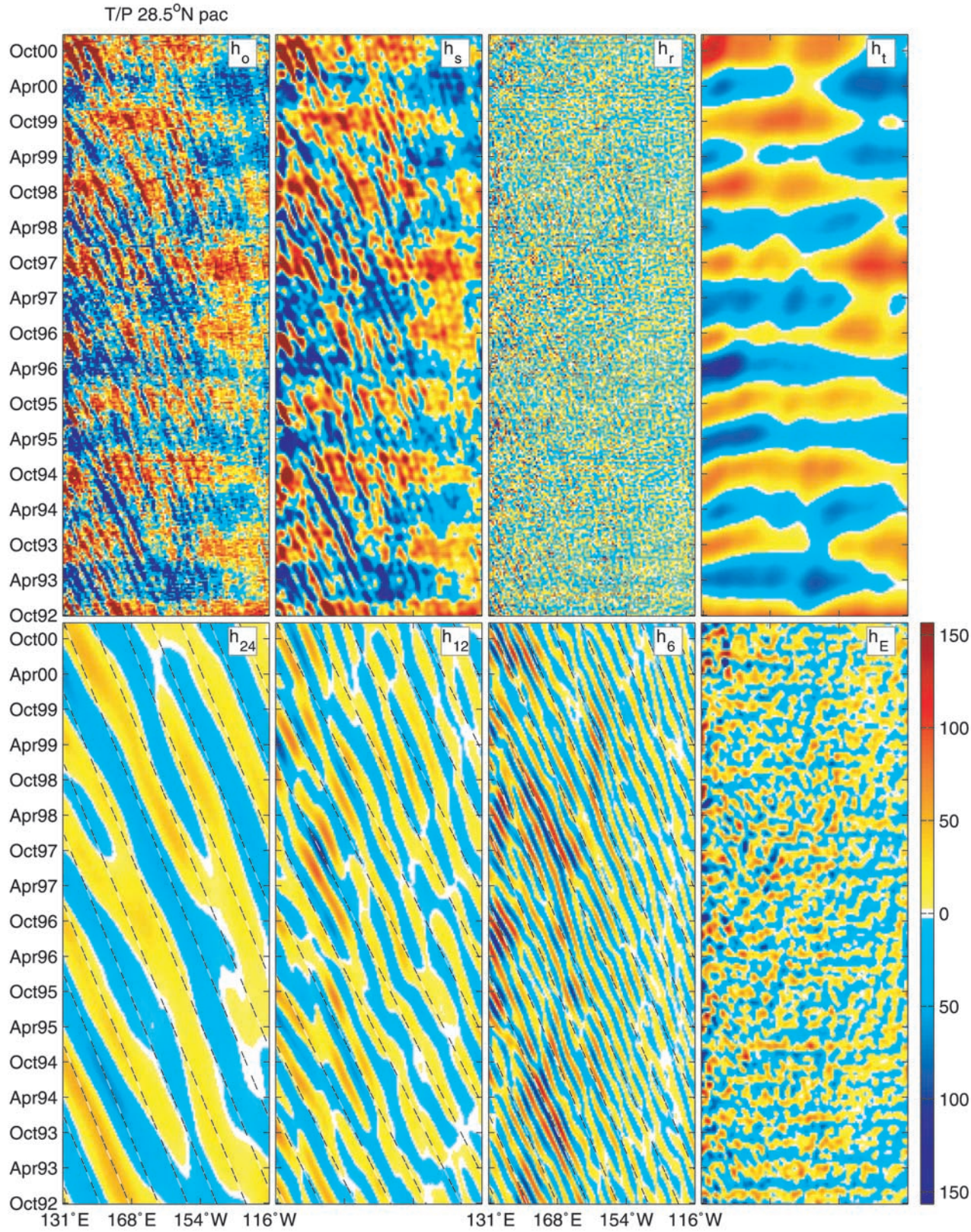

Figure 2. Original (η_o), sum of filtered (η_s), residual (η_r), and filtered sea surface height anomaly fields (η_t, η_{24}, η_{12}, η_6, and η_E), as in equation (3) at 28.5°N in the Pacific, in mm. Dash-dot lines are estimates for mean zonal phase speed.

Figure 3. Latitudinal distribution of the mean c_p (top left), P (center left), L (bottom left), A (top right), V (center right), and S/N for the Pacific ocean. Logarithmic (linear) axes are blue (black). Values from ZW and CS are shown for comparison.

T, L, A, V and S/N) and their respective error margins were estimated for all latitudes in Table 2 in the three basins for the six wave components of equation (3), what makes a total of 925 zonal-temporal diagrams. Each diagram has an average of 49 data blocks, in a total of 45,325 parameters. The presented data are greatly reduced by traditional statistical methods to make their interpretation feasible.

[27] Global estimates of the mean wave parameters are shown in Figures 3, 4, and 5 as a function of latitude. The c_p estimates in the top left panel are zonal and temporal averages for each component. The results from CS based on altimeter data are indicated by × (CS in the legend), the standard linear theory results are indicated by × (ST in the legend) and altimeter based results from ZW are indicated by + (ZW in the legend). To provide a meaningful comparison the estimates labeled "linear theory" are the same used in CS. The ZW c_p estimates are plotted with a color code that matches the closest frequency band from this study.

[28] For each component L and T are different. All parameters are estimated from data blocks that measure L by T, thus the averages are taken over a variable number of estimates for each latitude and basin. Components with short (long) T and L have averages taken over a large (small) number of samples. The averages shown in Figures 3, 4, and 5 are calculated in two steps. First the

Figure 4. Similar to Figure 3 for the Atlantic ocean.

mean and standard deviation are calculated over all samples. In the second step, the mean and standard deviation are recalculated without the samples that were outside the 95% confidence level (c.l.) or explained less than 3% of the total variance. In average, 24 (±12)% of the measurements are excluded by these criteria. This average does not vary significantly among the three basins. This precautionary measure is intended to prevent the introduction of biases from regions where the presence of waves is unclear.

[29] The propagation of Rossby waves is limited within critical latitudes, poleward of which no propagation is possible [*Mysak*, 1983]. The critical latitude depends on the frequency, with higher frequencies confined closer to the Equator. Therefore, at high latitudes only the low-frequency ocean response will be in the form of Rossby waves. The wavelengths decrease poleward faster than the decrease in T/P track separation; the higher the latitude, the worse the relative resolution of T/P for a given component of Rossby waves. Thus, besides the critical latitude threshold the observations are also limited by altimeter sampling. Additionally, the size of the filter depends on T and L and as the latter decreases poleward, so does the filter size and its skill. Thus, for a given component the S/N (Figures 3, 4, and 5, bottom right) tends to be lower at the highest latitudes. Tests with no latitudinal thresholds showed that poleward of the latitudes shown in Table 2 c_p, T and L estimates become erratic, because either the T/P has insufficient zonal resolution or a critical latitude has been reached. Due to these limitations the unambiguous determination of critical latitudes is not possible.

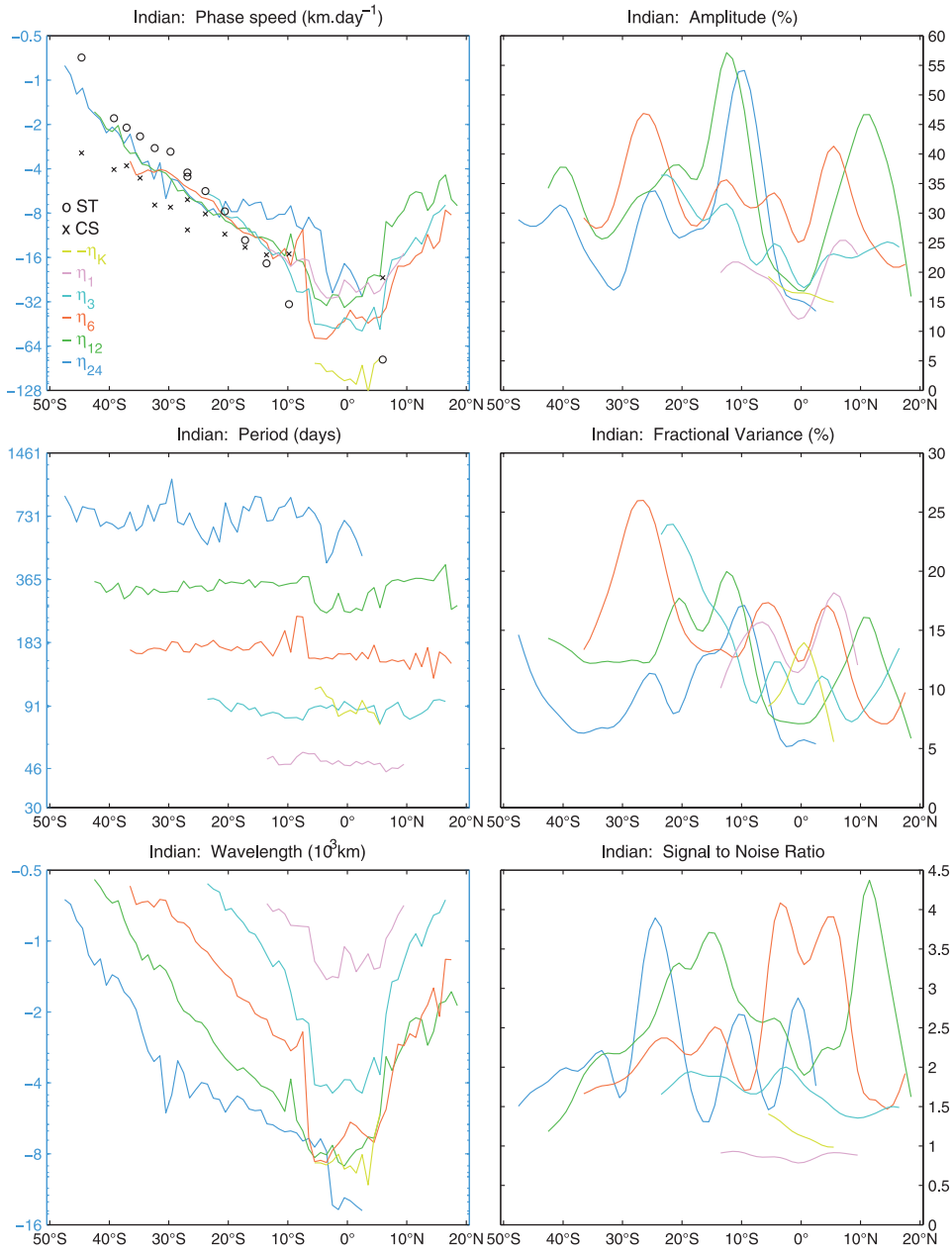

Figure 5. Similar to Figure 3 for the Indian ocean.

[30] In general, c_p has the smallest ME (Table 1) compared to T, A, and L. This is due to the Radon transform method which has an embedded integration step that decreases the error by averaging a large number of samples. In a similar comparison, A has the largest ME because it reflects how well a sinusoidal surface fits the filtered data that is not necessarily sinusoidal. The global root-mean-squared (rms) amplitude distribution for each component is shown in Figure 7. Unlike A the RMS amplitude does not depend on the waveshape or continuous phase propagation. Although only global averages are presented, SD and ME are estimated for every data block and therefore are functions of latitude, longitude, and time. SD and ME tend to increase poleward because of the decrease in zonal dimension of the data blocks. For the same reason SD and ME tend to increase as periods decrease. An equivalent observation can be made with respect to the S/N ratio in Figures 3, 4, and 5, bottom right.

4.3. The Phase Speed

[31] Rossby waves are the main mechanism of transport of energy across oceanic basins. In this context c_p sets the timescale for the energy introduced in the eastern side of the basin to reach the opposite margin. On a broader sense, c_p sets the response time for the oceanic gyres to react to changes in the atmospheric forcing. The importance attributed to the estimation of c_p in the recent literature derives from its possible role as an indicator of wind forced waves.

[32] Furthermore, the variability of c_p potentially suggests what factors modify the background PV gradient at a

Table 1. Meridional Average of the Standard Deviation and Measurement Error (95% CI) of c_p, t, a, and l Associated With the Data Shown in Figures 3, 4, and 5[a]

		Pacific		Atlantic		Indian	
		SD	ME	SD	ME	SD	ME
η_{24}	c_p	21	4	21	4	21	4
	T	22	4	21	4	21	5
	A	36	21	39	23	30	42
	L	21	9	13	6	18	10
η_{12}	c_p	21	3	20	3	21	4
	T	17	2	15	2	16	2
	A	39	13	34	15	35	21
	L	17	5	14	5	15	6
η_6	c_p	26	2	23	2	23	5
	T	19	2	17	2	17	2
	A	50	11	35	14	35	22
	L	21	4	19	5	18	6
η_3	c_p	25	3	23	4	26	10
	T	18	2	16	4	19	4
	A	49	12	36	18	38	28
	L	21	4	19	6	21	8
η_1	c_p	26	3	24	4	26	8
	T	19	5	20	8	19	9
	A	45	14	43	21	41	31
	L	22	4	21	8	21	10
η_K	c_p	34	4	30	5	30	8
	T	29	6	25	10	29	9
	A	43	18	30	30	28	37
	L	29	2	25	5	23	4

[a] All values are percentiles relative to the measurement.

given location and time when contrasted with numerical model results. The c_p can also be used as a diagnostic variable for ocean models, since it controls the flux of potential energy on the large scale and low frequency spectral band across oceanic basins. Next, the estimated c_p is compared to published values obtained at several locations, followed by a discussion of the relevant methodological differences.

[33] Most values of c_p shown in Figure 4 for η_6 and η_{12} are statistically identical to those by *Polito and Cornillon* [1997]. This is expected since the methodologies are similar and approximately half of the T/P time series is common to both studies. Significant differences are observed for η_{12} at 2.5°N and 7.5°N, as their c_p estimates are significantly faster. There are two factors that can cause this discrepancy. One is that the 10° zonal length of their data block is short compared to the local wavelength of $\sim 5 \times 10^3$ km associated with η_{12}. However, a similar comparison of c_p estimates for η_6 does not show significant discrepancies because η_6 has a relatively shorter wavelength. The other reason for the η_{12} differences relates to the method used to remove the seasonal signal. A sinusoidal least-squares fit leaves a nonpropagating residual signal since the annual cycle is not exactly sinusoidal. The phase speeds are estimated based on the alignment of patterns in $\eta(x, t)$ diagrams. The seasonal cycle appears as a horizontal pattern that goes across the whole basin at a given time and therefore has an infinite phase speed. If a residual of the seasonal signal is left in the data this residual may skew the Radon transform toward high phase speeds.

[34] The values of c_p from *Périgaud and Delecluse* [1992], based on Geosat data, for 10°S and 15°S, are −16 and −8 km/day, respectively. In Figure 5 a value of −11 km/day is found for 9.5°S and −12 km/day at 14.5°S. The differences are significant relative to the average error margins in Table 1. Our c_p at 10°S is relatively low while at 15°S it is relatively high. The annual signal in this region is very clear and reaches a S/N of more than 4. Therefore, filter contamination is quite unlikely to be the cause of these discrepancies. Since the two studies cover different periods, it is possible that the meridional slope of the pycnocline has changed and that would result in different distributions of phase speed with latitude.

[35] *Wang et al.* [1998] presented observations of long, first mode baroclinic Rossby waves at 25°S in the Pacific. They reported significant biannual and 9 to 10 month signals, both with phase speeds statistically identical to those in Figure 3 (−5.5 to −6 km/day). Our results show biannual, annual and semiannual signals of similar A, with a slightly smaller annual signal. The S/N ratio is higher for the annual component and V is larger for the semiannual. The discrepancy in relation to the annual signal is probably related to the different filtering techniques. This study uses a 2D filter as opposed to the two 1D (zonal dimension and time) used by *Wang et al.* [1998]. The use of 2D filters has two main advantages. One is that each output data point obtained from a 2D filter is calculated based on a significantly larger number of input data points in comparison with two 1D filters of the same length. This results in smaller statistical fluctuations and thus a better performance. The second advantage is that two 1D filters are insensitive to propagation. The phase obtained at time t is independent from the phase obtained at time $t + 1$. Tests indicate that two 1D filters are prone to generate phase breaks while 2D filters result in a more continuous phase propagation. It is possible that part of their annual signal was removed together with the seasonal signal by the 1D filters. This can bias T toward the next (semiannual) spectral peak.

[36] The estimated c_p in Figure 3 is in most cases within the error bars of the ZW results with the following exceptions. Their mean c_p estimates at 19°N in ZW area 2 (210°E to 250°E) for periods close to 90 days (75, 86, and 101 days) are significantly slower than our zonal average. Even if the average c_p is calculated within area 2, our results (−8 km/day) are still higher than the average of −5 km/day of ZW. However, if the 66-day wave is included, their mean c_p becomes identical to ours. Another large difference occurs for the 345-day wave on their area 4 (22°N). In this instance the error bars associated with the ZW estimates, when translated in terms of c_p, encompass all our estimates for this latitude. A direct point-by-point comparison with ZW cannot be made because often the

Table 2. Latitudinal Thresholds for Each Component

	Indian	Pacific	Atlantic
η_{24}	−47.5°, 2.5°	−49.5°, 51.5°	−48.5°, 47.5°
η_{12}	−42.5°, 18.5°	−42.5°, 40.5°	−41.5°, 42.5°
η_6	−36.5°, 17.5°	−32.5°, 34.5°	−32.5°, 34.5°
η_3	−23.5°, 16.5°	−24.5°, 26.5°	−23.5°, 24.5°
η_1	−13.5°, 9.5°	−13.5°, 14.5°	−10.5°, 13.5°
η_K	−5.5°, 5.5°	−3.5°, 5.5°	−3.5°, 5.5°

Table 3. Comparison of Ensemble Average Phase Speeds for the Pacific Within 3.5° of the Equator[a]

	c_p	c_{pT}	c_{pi}	m
η_{24}	−35 ± 10	−52 ± 26	−43 ± 43	3
η_{12}	−42 ± 5	−52 ± 26	−43 ± 43	3
η_6	−110 ± 34	−86 ± 17	−95 ± 17	1
η_3	−59 ± 19	−95 ± 43	−69 ± 26	2
η_1	−37 ± 11	−52 ± 26	−43 ± 43	3
η_K	160 ± 54	233 ± 78	199 ± 26	–

[a] Here, c_p refers to the current study. c_{pT} and c_{pi} refer to T/P-based and in situ (TAO moorings) based estimates, respectively, of phase speed from *Boulanger and Menkes* [1995]. The phase speeds can be associated with different meridional modes m.

frequency and wavelength bands are not the same, and even when the central frequencies are similar, the bandwidths differ. Another important methodological difference is that both the geographic area and the time series used in these studies are different. The relevance of these differences is demonstrated by the spatial and temporal variability of c_p (Figure 1).

[37] Because of these differences a point-by-point comparison does not provide as much insight as a broad, global comparison. Within this more general framework both results (ours and ZW) indicate that the standard linear theory (ST) provides a good approximation for most of the observed phase speeds (the c_p values for the ST in Figures 3, 4, and 5 are the same used in CS).

[38] The linear theory predicts a c_p that decays rapidly with frequencies higher than one cycle per 100 days. In ZW the c_p associated with these high frequency signals is too high compared with the linear dispersion curve, but is similar to the c_p associated with lower frequencies. We do not present results on these frequency bands at many of the latitudes studied by ZW. As latitudes increase the wavelengths that correspond to the higher Rossby wave bands reduce to less than twice the T/P track zonal separation. Therefore, it is impossible to resolve the waves with the method used here. In the latitudes where a comparison within the high-frequency band is possible our results are similar to those in ZW.

[39] Table 3 compares the present results for the ensemble mean of c_p and the ensemble mean of the standard deviation of c_p in the Pacific within 3.5° of the Equator with those reported by *Boulanger and Menkes* [1995]. The η_6 mean excludes the point at 1.5°N due to contamination. Inspection of the $\eta_6(x, t)$ diagram for 1.5°N (not shown) indicates that at this location the filter failed to separate the westward propagating semiannual Rossby wave signal from basin-wide signals with a 60 day period. Table 3 indicates which meridional wave mode identified by *Boulanger and Menkes* [1995] is closest to the present phase speed results. This comparison suggests that the equatorial Rossby waves are generally not of the first meridional mode. In this region the η_K, η_6 and η_1 components are the dominant wave signals in terms of V (Figure 3). Alternatively, it is possible that the different phase speeds among the several Rossby wave components for the same latitude may be due to different baroclinic modes or to coupling between ocean and atmosphere or to advective processes (Doppler effect).

[40] In the three basins the S/N ratios for the η_K and η_1 components are between 0.6 and 1.1 (lower right plot of Figures 3, 4, and 5). This precludes any strong conclusions based on these two components. However, the S/N ratios are low for different reasons. For η_1 the average S/N is low because the TIWs are an intermittent phenomenon. For η_K the probable cause for the low S/N is that a single spectral band is unable to accurately resolve the equatorial Kelvin wave signal.

[41] Except for the equatorial region, the c_p results in Figures 3, 4, and 5 are statistically identical to the ST. However, there is an average bias of ∼25% toward high speeds, poleward of 30° in the three basins. These differences are significantly smaller than the factor of 2 or more between ST and the CS observations. The relative discrepancies between the present estimates and those in CS also tend to increase at high latitudes. For instance, the estimated c_p at 28.5°N (Figure 2) in the Pacific is consistent with both the linear theory for long first-mode baroclinic Rossby waves and with the recent ZW results, but significantly lower than those in CS. In fact, our estimates are generally lower than those of CS in the mid to high latitudes of all basins. Two main methodological differences are suggested as the probable causes for this difference. The first and most important is that the CS estimates of c_p are, as noted by ZW, based on a broadband signal while the present work treats several spectral bands individually. The second regards the removal of the non-propagating signals. The annual component has often the clearest and most energetic signal of all Rossby waves. The ubiquitous seasonal signal appears as horizontal bands in zonal-temporal diagrams such as in Figure 2. This pattern tends to bias the estimates of annual Rossby wave c_p that are based on the Radon transform toward high absolute values.

[42] In the equatorial region between 9.5°S and 9.5°N the values of c_p associated with η_{24}, η_{12} and η_1 are similar and depart significantly from the c_p associated with η_6 and η_3. This c_p differentiation may be due to the modal structure of these waves or, in some cases, problems with the filter.

4.4. Other Parameters

[43] The periods that correspond to the center of each band are input parameters that remain constant throughout the filtering process. Nevertheless, the passbands are wide enough to provide for some variability in the period within each band (Figures 3, 4, and 5). As expected, the mean period is close to the center of each band. However, there are noticable departures from the input period, regarded as an indication of problems with the filter.

[44] The T associated with the η_{24} component in the Atlantic basin (Figure 4) shows the influence of a stronger high-frequency signal upon a weaker η_{24} at 0.5°N and 5.5°N. In both Atlantic and Pacific basins, within 1.5° of the Equator, the period of η_6 departs significantly from 180 days. In these cases the filter is unable to isolate the semiannual equatorial Rossby wave signal. The contamination occurs because when phase speeds reach large values ($|c_p| \geq 1$ m/s) their pattern on the $\eta(x, t)$ diagrams with the resolution used here become almost horizontal, with a wavelength comparable to the basin width. The c_p is estimated based on the angle of inclination of the patterns in $\eta(x, t)$, via Radon transform. For fast waves these angles differ by a few degrees.

This results in a significant decrease in the skill of the filter to separate fast westward-propagating, nonpropagating and fast eastward-propagating signals. Figure 6 is similar to Figure 2 but for the equatorial Pacific, and displays η_6 signals as nearly horizontal bands that suggest contamination by fast equatorial Kelvin waves. The inspection of T and L associated with η_K reinforces this suggestion. Consequently, while the amplitude of η_6 is overestimated the amplitude of η_K is underestimated at those latitudes.

[45] Waves of the equatorial Indian ocean have periods close to the set periods, with one exception for η_6 near 8.5°S where it gets closer to annual. A simple explanation based on filter contamination is not very convincing because η_6 is robust in terms of both V and A (Figure 5). It is possible that in this particular location η_6 represents a nearly annual baroclinic wave of the second mode. Based on S/N estimates the clearest signal is η_{12} and its c_p is indicative of long equatorial first mode baroclinic waves. The substitution of $n = 2$ in equation (3) yields $c_p = -12$ km/day, similar to the -11 km/day observed for η_6. Alternative explanations could include advection and atmospheric forcing as the cause of the anomalous phase speed. A detailed study of this particular region escapes the objectives of this study.

[46] In the latitudinal bands that bracket the eastward flowing extension of the subtropical gyres the period of η_{12} tends to be less than one year. For instance, between 35°N and 40°N in the Atlantic the period is approximately 300 days, statistically distinct at 95% c.l. from 365 days. A 9 month periodicity in the intensity of the meanders of the Gulf Stream was reported by *Lee and Cornillon* [1996] and the hypothesis of a link between this period and Rossby wave forcing was discussed. Their hypothesis is confirmed by the present results, if one takes into account the error margins associated with both estimates.

[47] The fractional variance V attributed to each wave component is shown in Figures 3, 4, and 5 (middle right). Most waves in the Atlantic have two local maxima at or near 30.5°S and 33.5°N, but this is not observed for the Indian and Pacific basins. These two maxima in the Atlantic are also noticable in the plots of A (top right) for η_6 η_{12} and η_{24}. The relatively small zonal extension of the Atlantic and the exclusion of data blocks with relatively low variance intensifies the influence of these two current systems in the zonal average. These maxima are indicative of the interaction between western boundary currents, their energetic eddies and meanders, and Rossby waves. Zonal-temporal diagrams similar to Figure 2 for the Atlantic suggest that the waves that come from the eastern basin perturb the current. This contributes to the formation of eddies and meanders whose energy apparently radiates toward the middle of the gyre and reinforce the wave field.

4.5. Amplitude

[48] Figure 7 shows the RMS amplitude (in mm) of each component of equation (3). The color codes are different and can be used to quantify the relative intensities of these fields. It complements Figures 3, 4, and 5 because the mean A values plotted in these three figures are obtained by least squares fit of a sinusoidal surface on a subset of the filtered data that excludes data blocks with weak signals. The RMS amplitude in Figure 7 includes these data and allows for the visualization of the geographical distribution of power among the various spectral components.

[49] The tropical Pacific has the highest η_t amplitudes because of the ENSO signal in addition to the seasonal signal. In this region η_t accounts for over 70% of the variability. Only the strong seasonality that characterizes the midlatitudes has a similar amplitude over the western boundary currents due to the enhanced surface heat fluxes.

[50] The South Atlantic has the least intense wave signals of all basins. In contrast, the North Pacific has the strongest Rossby wave signals in all components. In terms of meso-scale eddy activity all basins have a more equitable share of energy, with the South Pacific in the low end and the Southern ocean in the high end. The western boundary current retroflection regions have a strong influence in the Rossby wave fields. The Kuroshio, Agulhas, Gulf Stream, and Brazil currents can be easily located in the η_{24}, η_{12}, and η_6 maps in Figure 7. In addition to these locations, η_{24} is particularly strong in the equatorial Indian ocean along 8°S. In the Pacific, between 5°S and 25°S η_{24} has a significant amplitude and is responsible for approximately 20% of the total variance. In the north Pacific at the same latitudes the high amplitude of η_{24} is confined near the Philippine Sea. The annual η_{12} and semiannual η_6 are the most prominent Rossby waves signals. While the amplitude of η_{12} is higher than that of η_6 in the Atlantic and Indian oceans, it is not the case in the Pacific. A particularly intense local maximum in η_6 is found east of the Luzon Strait (~22°N, 125°E).

[51] Before proceeding with the description of the η_3, η_1, and η_K fields it is necessary to reiterate that if the period decreases the filter size and skill also decrease. Consequently, the RMS amplitude tends to be overestimated as the passbands includes more noise. Rossby waves with a period of approximately 3 months are very intense in the northern tropical Pacific along 20°N. In the southern Pacific at a similar latitude the signal is not as intense as in the southern Indian ocean. The η_1 maximum in the equatorial Pacific is indicative of TIWs [*Legeckis*, 1977]. These signals have a period of approximately 45 days which is longer than some of the previously reported TIWs [*Qiao and Weisberg*, 1995]. However, c_p is within the range of previously published observational results based on several independent sensors.

[52] Given the 10-day repeat cycle of T/P it is plausible that our results bracket just the low frequency part of the TIW spectrum. This is qualitatively confirmed by the presence of a small amount of high frequency wave-like patterns in the residual η_r. η_r is the difference between the sum of the filtered signals and the original signal in Figure 6.

5. Summary and Conclusions

[53] A method based on 2D FIR filters [*Polito et al.*, 2000] is used to separate the T/P residual sea surface height $\eta_o(x, t)$ into zonally propagating and nonpropagat-

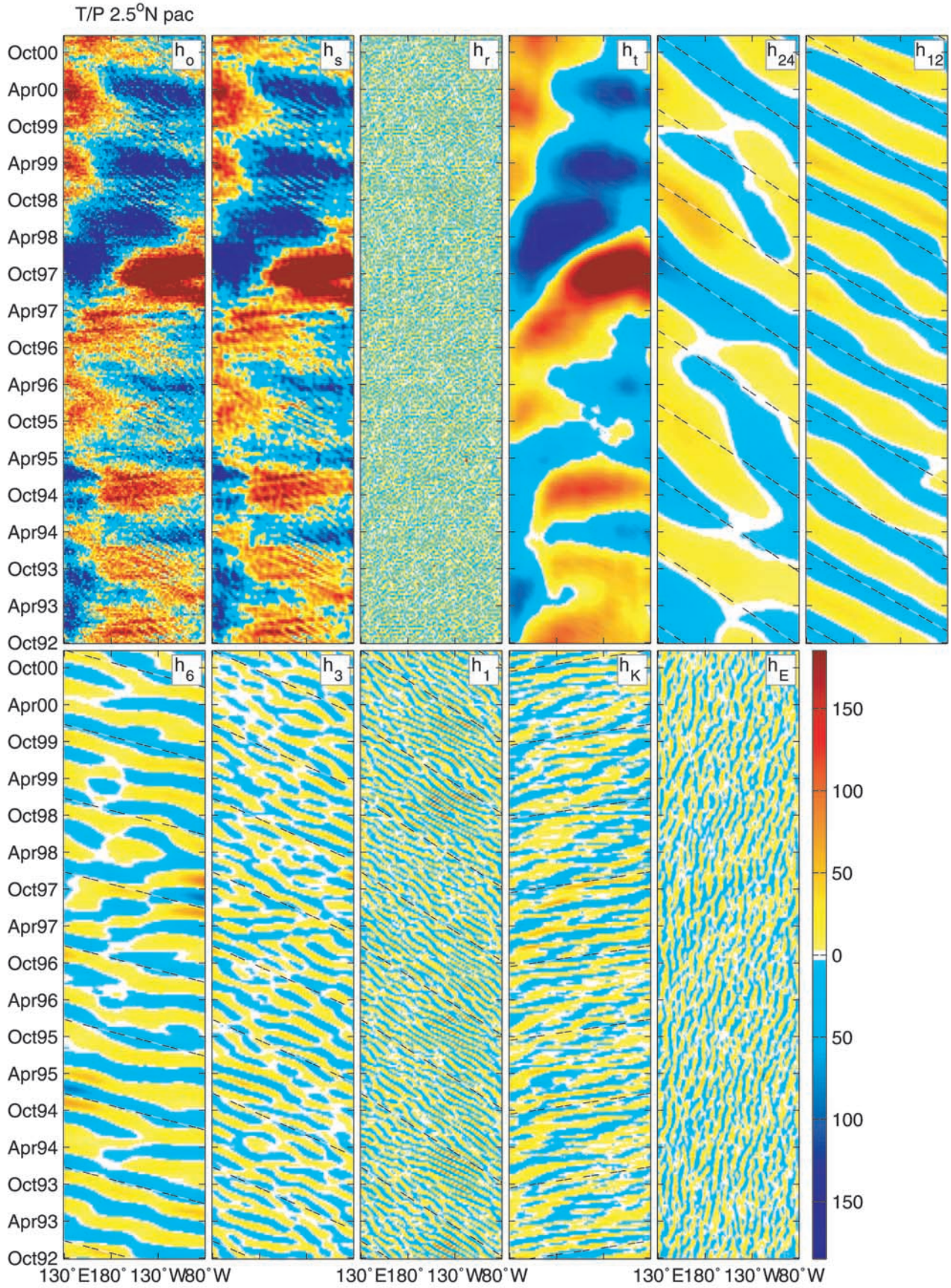

Figure 6. Similar to Figure 2 for 2.5°N in the Pacific.

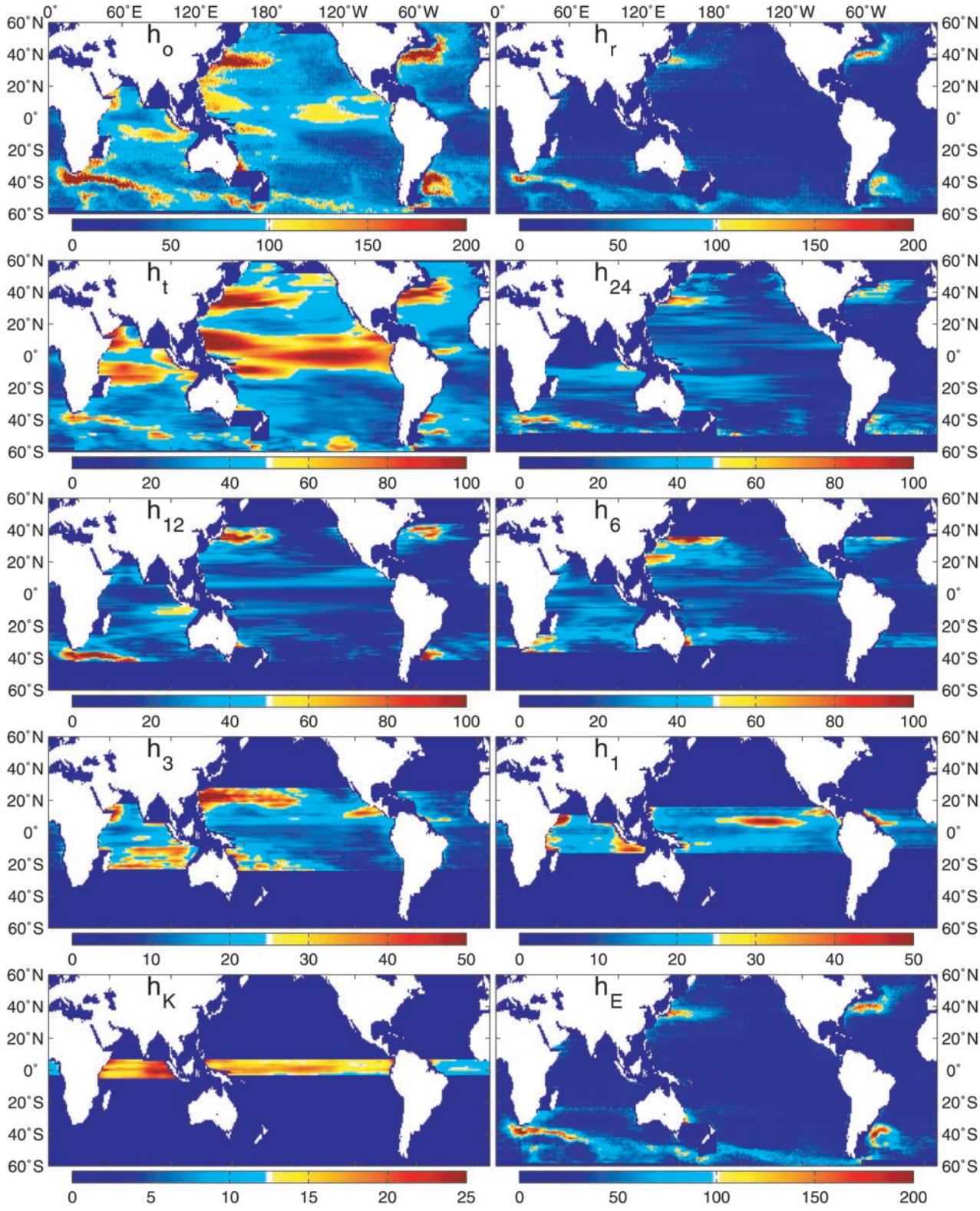

Figure 7. Rms amplitude of the filtered sea surface height components in mm, as in equation (3). The filtered signals are latitudinally limited (Table 2).

ing components, with particular attention to long baroclinic Rossby waves. The filters do not significantly alter the phase or its propagation speed in relation to the original data (Figures 2 and 8).

[54] At each degree of latitude the filtered data are divided into blocks and the wave parameters c_p, T, L, A, V, and S/N are estimated within each block. These parameters are therefore a function of longitude and time at each

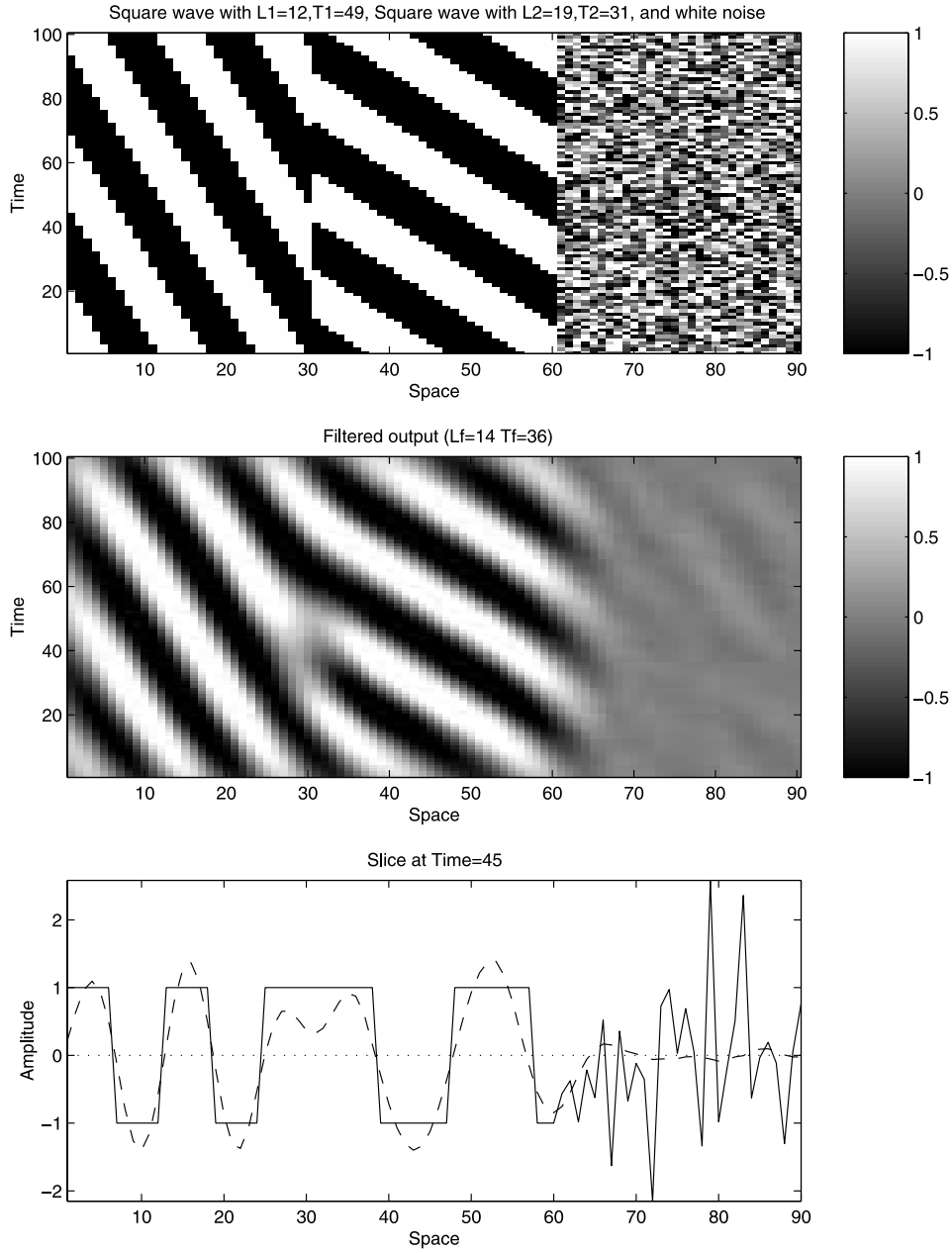

Figure 8. Top: Input data with two square waves and white noise. Middle: Filtered data show the preservation of phase, period, wavelength, and phase speed. Bottom: Results for Time = 45 with the original data (-) and the filtered data (- -).

latitude. The mean values for each latitude are shown in Figures 3, 4, and 5. The overall mean of the ME and SD are presented in Table 1.

[55] The waves are likely to be aliased [*Parke et al.*, 1998] poleward of the latitudinal thresholds (Table 2) of each component due to the lack of zonal resolution. Therefore, the location of critical latitudes cannot be determined in this study.

[56] The c_p estimates in the North Atlantic are in close agreement with *Polito and Cornillon* [1997]. The discrepancies that occur at low latitudes for the annual component are mainly a consequence of methodological differences. They used a data block with a fixed size that becomes smaller than the annual waves at $\sim$12°N. This, in conjunction with the possible remainder of the seasonal cycle, biases c_p estimates toward high values.

[57] A comparison of results with *Wang et al.* [1998] at 25°S in the Pacific shows statistically identical values for c_p while the spectral composition is slightly different. Our study shows signals with approximately 6, 12, and 24 months while they report signals with approximately 9 and 24 months. It is plausible that part of their annual signal was removed together with the seasonal signal biasing the period toward the semiannual component.

[58] In most cases our c_p estimates are within the error bars of those in ZW, including some of their high-frequency cases that depart from the linear dispersion curve. However, their high-frequency results in areas 5, 6 and 7 ($\sim$28°N, 33.5°N and 38°N) have no counterpart in this study. In these cases L is smaller than twice the T/P track separation and thus below the latitudinal thresholds shown in Table 2.

[59] In the Pacific, the average c_p within 3.5° of the Equator are similar to those obtained by *Boulanger and Menkes* [1995] (Table 3). A clear assessment of the issues related to equatorial Kelvin waves is not possible due to the small signal-to-noise ratio associated with η_K. Tropical instability waves were analyzed in detail by *Polito et al.* [2001] and their results corroborate those in Figure 3. In the Indian ocean near 8.5° S there are indications of a second mode baroclinic Rossby wave of semiannual period. Outside the equatorial region all the components are first mode baroclinic as indicated by their average c_p. The indication of multiple modes in the equatorial regions is based on the variation of phase speed among the several components. Alternatively, this variation could be caused by interaction with the atmosphere or with local currents. More solid conclusions demand further investigation including other sources of data (e.g., hydrocasts, sea surface temperature, and marine winds).

[60] The most important scientific contribution of this study is the observation that in a global average sense the oceanic Rossby waves behave approximately like free waves. Our estimates of the average c_p are closer to the standard theory compared to those in CS, particularly at mid to high latitudes. There is a bias toward high values poleward of $\sim$30° noticable in Figures 3, 4, and 5. This bias is in average approximately 25% much lower than the factor of 2 obtained by CS, and lower than the $\sim$50% from the theoretical work of *Killworth et al.* [1997]. The most important methodological difference between CS and this study is that here the spectral bands are treated separately. This allows for a more precise estimation of the phase speeds [*Zang and Wunch*, 1999]. The 2D FIR filters can distinguish propagating from nonpropagating signals and therefore are well suited to separate the seasonal signal from the wave signal. By comparison, it is possible that the remainder of the seasonal signal has biased the CS c_p estimates, which were based on the Radon transform, toward high values.

[61] Outside the equatorial region the c_p of the Rossby waves is indicative of the first baroclinic mode. An implication of this result is that the waves observed by the altimeter are a surface manifestation of the vertical displacement of the main thermocline. Therefore these passage of these waves changes the local amount of heat stored in the water column. The heat capacity of the upper layer of the ocean surpasses that of the atmosphere by many orders of magnitude. Therefore these waves have a potentially important influence on the local climate variability.

[62] Analysis of the period of the filtered components in the equatorial region shows that a relatively weak component can be contaminated by a dominant signal. Contamination occurs in the equatorial region because the zonal-temporal patterns generated by fast waves are very similar, regardless if they propagate East, West or do not propagate at all.

[63] In the latitudes that correspond to the eastward branch of the big circulation gyres the period of the annual Rossby waves tends to be lower than one year. This result is evidence that the 9 month periodicity in the intensity of Gulf Stream meanders is caused by Rossby waves [*Lee and Cornillon*, 1996].

[64] Many curious aspects of the wave signals depicted in Figure 7 are left as future work due to keep this article concise. For instance, intense TIWs with a period of approximately 45 days are observed in the eastern tropical Pacific (η_1 in Figure 7) and were confirmed by *Polito et al.* [2001]. Rossby waves with a 90 days period are dominant in the southern Indian basin with a significant amplitude in the tropical North Pacific. A strong semiannual maximum is observed near 20°N in the Pacific apparently spreads from the Luzon Strait. The η_{12} is most intense over the regions where the western boundary currents retroflect. However, significant η_{12} amplitudes are also observed in the tropical Pacific near the coast of Central America and in the southern Indian ocean west of the Timor Sea. The main differences between the amplitude distributions of η_{12} and η_{24} are in the southwestern Pacific and southeastern Indian Basin where η_{24} has significant maxima.

Appendix A: Detailed Methodology

[65] The need for filters arises from the difficulties inherent to the measurement of 2D phase propagation of waves with a broad spectrum. Finite impulse response (FIR) filters operate through convolution in the time-space domain as opposed to frequency-wave number domain used in Fourier analysis. In Fourier analysis the data are separated into a sum of sinusoidals and each component has a single period (or wavelength), or a single spectral line and is scaled by a fixed amplitude. The sinusoidal shape allows for analysis in the time domain and in the frequency domain. In the FIR filter method each filtered component covers a range of periods (or wavelengths), or a spectral band, instead of a spectral line. Both amplitude and period can vary, the latter is chosen a priori and is limited by the bandwidth. No functional shape is assumed and the data are always treated in the time domain. This makes the filter design process more intuitive thus easier to adapt to oceanographic applications in which two out of the three parameters, c_p, T, and L, are known to be within a certain range. The filter parameters are adjusted to bracket the spectral bands related to previously observed physical processes (e.g., seasonality, Rossby and Kelvin waves). This is an advantage in relation to classical Fourier analysis and complex empirical orthogonal functions, since both methods do not allow for such adjustments. A thorough description of the FIR filters used in this study is given by *Polito et al.* [2000].

A.1. Filters

[66] Figure 8 shows an example of the filter performance. In this example the top panel shows an artificially built input data set composed by two square-waves and a random noise field assembled side by side in a single matrix. This matrix is filtered at once with a single FIR filter that has the

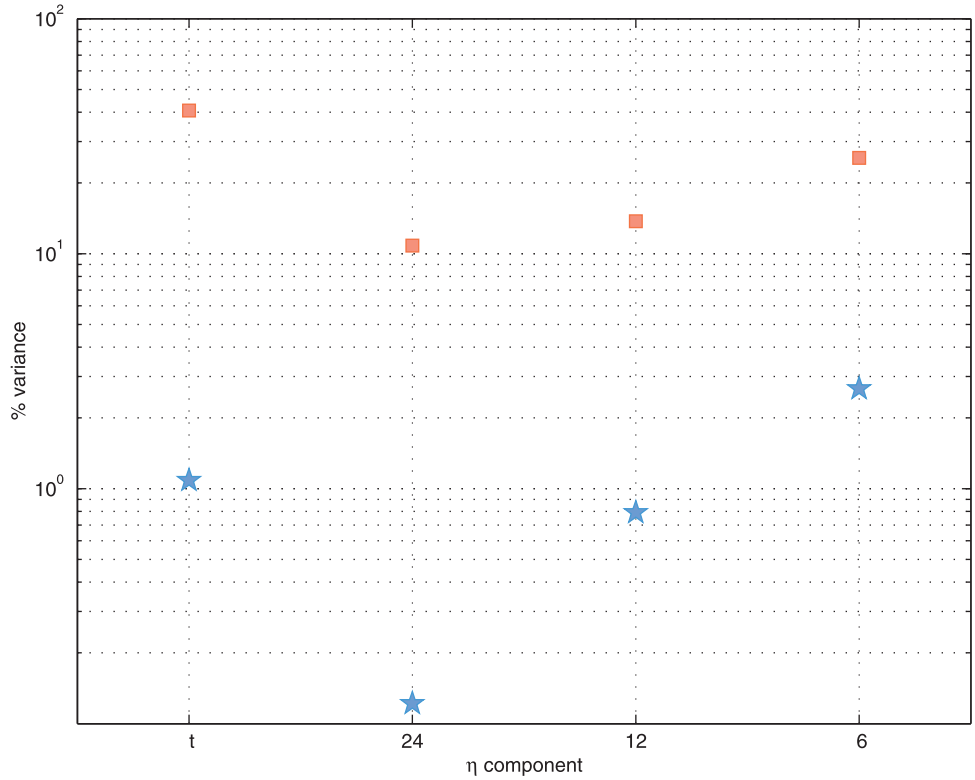

Figure 9. Fraction of variance (%) explained by the filtered components of the T/P altimeter data (squares) in comparison with random white noise (stars), at 28.5°N in the Pacific.

same tapered cosine shape as the one used for the T/P data. The filter period, wavelength, and phase speed are, in arbitrary units, $T_f = 36$, $L_f = 14$ and $c_{pf} = 0.39$. These parameters are different from those used to build the input data, namely $T_1 = 49$, $L_1 = 12$ and $c_{p1} = 0.24$ for the leftmost wave and $T_2 = 31$, $L_2 = 19$ and $c_{p2} = 0.62$ for the central wave. The spectral band of the filter is centered between the two wave signals and encompasses both of them. The filtered signal in the middle panel shows that the filter does not change the phase, period, length or phase speed of the original waves. The amplitude is mostly preserved, except at the borders and at the transitions between regimes (i.e., at Space = (0, 30, 60, 90) and Time = (0, 100)). The bottom plot shows results for Time = 45, with the original data as a continuous line and the filtered data as a dashed line. This time was chosen because it has a clear discontinuity in phase at Space = 30, between the two wave fields. This plot shows that the filtered wave has no particular shape. It shows also that its amplitude is close to 1, follows the original data in the two wave regimes, and tends to zero over the white noise regime.

[67] A brief overview follows, preserving the original *Polito et al.* [2000] notation. A series of FIR filters are successively applied to the $\eta_o(x, t)$ fields, one for each latitude and basin. The filters designed to capture non-propagating (η_t, η_E) signals are symmetric Gaussian functions while propagating signals (η_{24}, η_{12}, η_6, η_3, η_1, η_K) are filtered with asymmetric tapered-cosine functions. For non-propagating signals the wavelength is fixed, while for propagating signals it is obtained iteratively from successive estimations of the phase speed, since the filter periods are fixed. An extrapolation of the phase speeds from the standard theory from CS followed by one run of the filter are used to obtain initial value of the phase speed c_{p1}. The c_{p1} is initially the same for all components and all basins, and varies only with latitude. The process starts with filters based on c_{p1} and T. The filters are applied and from the filtered data a new c_p is obtained and replaces c_{p1}. The filter is redesigned, applied, and new c_p values are obtained to replace the old ones. The loop repeats until c_p converges to a stable value between $c_{p1}/2$ and $2c_{p1}$ (i.e., c_p changes less than 10%). This procedure minimizes the effect of the arbitrary choice of the initial c_{p1} which just needs to be within a factor of two of the "true" c_p.

[68] The filters are applied sequentially in the order shown in equation (3). The order is necessary because each data block used to obtain one filtered sample should have approximately zero mean because of the filter design. A large scale signal would make the small scale data block to have a nonzero mean and this would result in a biased output. More specifically, η_{24} is obtained from $\eta_o - \eta_t$, η_{12} is obtained from $\eta_o - \eta_t - \eta_{24}$, and so on. To avoid cross contamination between bands the correlated part of each band is removed from all other bands via least-squares fit. Spatial alias [*Parke et al.*, 1998] occurs when L is comparable to twice the zonal separation of T/P tracks. To avoid this problem the filter for each frequency was limited to a latitudinal band (Table 2).

[69] A series of tests were conducted to check the statistical significance of the filtered output. The results for 28.5°N in the Pacific are illustrated in Figure 9. A white random noise field with the same size and variance

as the T/P data is constructed and filtered exactly the same way as the T/P data. The fraction of variance explained by each filtered component, both for T/P and white random noise, is shown in Figure 9. The fractional variance of η_t is calculated in relation to the original signal η_o. This component is generally dominated by seasonality and in the present case it is nearly two orders of magnitude above the noise level. For all other components the fractional variance is relative to the signal used prior to the application of the filter. For example, the variance of η_{24} is relative to that of $\eta_o - \eta_t$, the variance of η_{12} is relative to $\eta_o - \eta_t - \eta_{24}$, and so on. This example is typical of midlatitudes and the Rossby wave components are approximately one order of magnitude above the noise level.

[70] Tests for the equatorial region (not shown) give similar results for all the components shown in Figure 9. At low latitudes T/P resolves waves with shorter periods, η_3, η_1 and, η_K. Their fractional variances are, respectively, 7, 2 and, 1.3 times larger than the ones obtained from white noise. Thus, at higher frequencies the results degrade. This is due to two factors. First, the ocean spectrum is not white. It has more energy in the low frequency bands, therefore the energy in the high frequency bands of the white noise are overestimated. Second, the for shorter periods the filters are smaller therefore less efficient. That results in a smaller signal-to-noise ratio for the high frequency bands (Figures 3, 4, and 5).

A.2. Wave Parameters

[71] The c_p is calculated in two instances. The first is within the iterations of the filter. The mean value of $c_p(y)$ for a particular latitude and basin is used in the iterations only to automatically adjust the filter. The filters are designed for a smooth transition between passband and stopband. This allows for natural variability in the filtered data. All the wave components of the filtered data are divided into data blocks that measure L by T. The natural variability is captured in the second instance when the final $c_p(x, y, t)$ is estimated within each of the data blocks of the filtered data. This is the c_p shown in Figures 3, 4, and 5. In both instances c_p is estimated with a modified Radon transform. The method [*Lim*, 1990] is explained in detail by *Polito and Cornillon* [1997], thus a brief explanation would suffice.

[72] The autocorrelation c (x_l, t_l) of η_o (x, t) is calculated for each data block as a function of zonal and meridional lags x_l and y_l. The advantage of the use of the autocorrelation instead of the height itself is that the autocorrelation has the same spectral information yet the random errors are considerably smaller. The matrix c is rotated around its origin in relation to a fixed pair of Cartesian axes. For each angle θ the sum p of c along the fixed vertical axis is calculated and divided by the number of points and yields the average $\bar{p}$. When θ is such that all the wave fronts in c are aligned with the vertical axis, the standard deviation $\sigma(\theta)$ of $\bar{p}$ is maximized. The tangent of this angle θ is an estimate of c_p ($c_p = L/T$).

[73] In addition to section 4.2, details of the wave parameter estimation follows. For each latitude and basin a set of parameters is estimated for every $\eta_i(x, t)$, where η_i is a data block of a given wave component of equation (3). The T and L are estimated by least-squares fitting sinusoidal functions at zero zonal and temporal lags of $c(x_l, t_l)$, respectively. The A is estimated by least-squares fitting a 2D sinusoidal surface with the estimated T and L directly to η_i. The RMS amplitude (Figure 7) is defined as the temporal standard deviation of $\eta_i(x, t)$ at each geographical location. The measurement error associated with T, L, and A estimates is the standard error of the least-squares fit. The RMS difference between η_i and the adjusted 2D sinusoidal yields the noise used for the estimation of S/N. This way to estimate A and S/N compares the filtered waves with a monochromatic sinusoidal shape with constant A, P, and L similar to that of the waves. However, the real waves are not necessarily sinusoidal neither monochromatic. Thus both A and S/N should be regarded as conservative estimates with a tendency toward low values. Furthermore, waves that are intermittent (TIWs are a good example) tend to have low average S/N ratios.

A.3. Error Estimates

[74] The variability in the estimates of c_p (and other wave parameters) at a given location is caused by instrument errors and natural variability. While the first depends on the instrument, orbit design, and method used for parameter estimation the latter depends on the local variations of the PV gradient, wind-forcing, and currents among other factors.

[75] The instrument error or the accuracy in the determination of η from the interpolated T/P data is set to $e = 30$ mm. From that the errors are propagated to each of the estimated parameters.

[76] The c_p is estimated from the angle θ corresponding to the maximum $\sigma(\theta)$ of the Radon transform $\bar{p}$. The error in θ should reflect how well defined this maximum is. To quantify this the error margins $e\sigma$ of $\sigma(\theta)$ are estimated as:

$$e_\sigma = \frac{\kappa e}{\sqrt{(n_b n_p)}},$$

where n_p is the average number of points used in the Radon transform for each angle θ. κ is the kurtosis of $\sigma(\theta)$ and compensates for $\sigma(\theta)$ not being exactly a normal distribution [*Press et al.*, 1989]. The n_b is the effective sample size [*Preisendorfer*, 1988] of $\bar{p}$ and is used because the process of filtering smooths the sample thus reduces the numbers of degrees of freedom:

$$n_b = \frac{1-\rho}{1+\rho},\ \rho = \frac{\sum_{i=1}^{n-1} \bar{p}(i+1)\bar{p}(i)}{\sum_{i=2}^{n} \bar{p}(i)^2}$$

[77] The 95% c.l. for θ (and c_p) is defined as the θ range corresponding to values of $\sigma(\theta)$ within $2e\sigma$ of the maximum. Notice that as $c_p = \tan(\theta)$ the error bars are not necessarily symmetric in relation to the mean. The error of T, L, and A are the standard least-squares fit errors based on the residual RMS difference between the fit and the filtered data within each data block.

[78] **Acknowledgments.** This study was performed at the Instituto Nacional de Pesquisas Espaciais (INPE), São Paulo, Brazil, and at the Jet Propulsion Laboratory, California Institute of Technology, under contract with the National Aeronautics and Space Administration (NASA). The study was jointly supported by the Coordenadoria de Observação da Terra of INPE, the Conselho Nacional de Desenvolvimento Científico e Tecno-

lógico (CNPq) and the Physical Oceanography, Earth Observing System Interdisciplinary Sciences Programs of NASA. The authors wish to express their gratitude to D. B. Chelton and X. Zang for kindly sending us their data, to O. T. Sato, and to the anonymous reviewers whose comments and suggestions were of immense help.

References

Benada, R., *Merged GDR TOPEX/Poseidon Users Handbook Version 2.0*, d-11007, Jet Propul. Lab. PO.DAAC, Pasadena, Calif., 1997.

Boulanger, J.-P., and C. Menkes, Propagation and reflection of long equatorial waves in the Pacific Ocean during the 1992–1993 El Niño, *J. Geophys. Res.*, *100*, 25,041–25,059, 1995.

Chambers, D. P., B. D. Tapley, and R. H. Stewart, Long-period ocean heat storage rates and basin-scale heat fluxes from TOPEX, *J. Geophys. Res.*, *102*, 10,525–10,533, 1997.

Chelton, D. B., and M. Schlax, Global observations of oceanic Rossby waves, *Science*, *272*, 234–238, 1996.

Cipollini, P., D. Cromwell, M. S. Jones, G. D. Quartly, and P. G. Challenor, Concurrent altimeter and infrared observations of Rossby wave propagation near 34° in the northeast Atlantic, *Geophys. Res. Lett.*, *24*, 889–892, 1997.

Gill, A. E., *Atmosphere-Ocean Dynamics*, *Int. Geophys. Ser.*, vol. 30, 662 pp., Academic, San Diego, Calif., 1982.

Herrmann, P., and W. Krauß, Generation and propagation of annual Rossby waves in the North Atlantic, *J. Phys. Oceanogr.*, *19*, 727–744, 1989.

Kessler, W. S., Observations of long Rossby waves in the northern tropical Pacific, *Tech. Memo. ERL PMEL-86*, 169 pp., NOAA, Seattle, Wash., 1989.

Killworth, P. D., D. B. Chelton, and R. A. de Szoeke, The speed of observed and theoretical long extratropical planetary waves, *J. Phys. Oceanogr.*, *27*, 1946–1966, 1997.

Lee, T., and P. Cornillon, Propagation and growth of Gulf Stream meanders between 75 deg and 45 deg *W*, *J. Phys. Oceanogr.*, *26*, 225–241, 1996.

Legeckis, R., Long waves in the eastern equatorial Pacific Ocean: A view from a geostationary satellite, *Science*, *197*, 1179–1181, 1977.

Lim, J. S., *Two-Dimensional Signal and Image Processing, Signal Process. Ser.*, vol. 16, 694 pp., Prentice-Hall, Old Tappan, N. J., 1990.

Lippert, A., and R. H. Käse, Stochastic wind forcing of baroclinic Rossby waves in the presence of a meridional boundary, *J. Phys. Oceanogr.*, *15*, 184–194, 1985.

Liu, W. T., X. Xie, P. S. Polito, S.-P. Xie, and H. Hashizume, Atmospheric manifestation of tropical instability wave observed by QuikSCAT and Tropical Rain Measuring Mission, *Geophys. Res. Lett.*, *27*, 2545–2548, 2000.

Mysak, L. A., Generation of annual Rossby waves in the North Pacific, *J. Phys. Oceanogr.*, *13*, 1908–1923, 1983.

Parke, M. E., R. L. G. Born, C. McLaughlin, and C. Tierney, Altimeter sampling characteristics using a single satellite, *J. Geophys. Res.*, *103*, 10,513–10,526, 1998.

Pedlosky, J., *Geophysical Fluid Dynamics*, 2nd ed., Springer-Verlag, New York, 1986.

Périgaud, C., and P. Delecluse, Annual sea level variations in the southern tropical Indian Ocean from Geosat and shallow-water simulations, *J. Geophys. Res.*, *97*, 20,169–20,178, 1992.

Polito, P. S., Observation of long first-mode baroclinic Rossby waves in the North Atlantic and their connection with wind forcing, Ph.D. thesis, 101 pp., Univ. of Rhode Island, Kingston, 1997.

Polito, P. S., and P. Cornillon, Long baroclinic Rossby waves detected by Topex/Poseidon, *J. Geophys. Res.*, *102*, 3215–3235, 1997.

Polito, P. S., O. T. Sato, and W. T. Liu, Characterization and validation of heat storage variability from Topex/Poseidon at four oceanographic sites, *J. Geophys. Res.*, *105*, 16,911–16,921, 2000.

Polito, P. S., J. P. Ryan, W. T. Liu, and F. P. Chavez, Oceanic and atmospheric anomalies of tropical instability waves, *Geophys. Res. Lett.*, *28*, 2233–2236, 2001.

Preisendorfer, R. W., Developments in atmospheric science, in *Principal Component Analysis in Meteorology and Oceanography*, edited by C. D. Mobley, Elsevier Sci., New York, 1988.

Press, W. H., B. P. Flannery, S. A. Teukolsky, and W. T. Vetterling, *Numerical Recipes, the Art of Scientific Computing (FORTRAN version)*, Press Syndicate of the Univ. of Cambridge, New York, 1989.

Qiao, L., and R. H. Weisberg, Tropical instability wave kinematics: Observations from the tropical instability wave experiment (TIWE), *J. Phys. Oceanogr.*, *100*, 8677–8693, 1995.

Qiu, B., W. Miao, and P. Müller, Propagation and decay of forced and free baroclinic Rossby waves in off-equatorial oceans, *J. Phys. Oceanogr.*, *27*, 2405–2417, 1997.

Rossby, C. G., On the mutual adjustment of pressure and velocity distributions on certain simple current systems II, *J. Mar. Res.*, *2*, 239–263, 1938.

Sato, O. T., P. S. Polito, and W. T. Liu, The importance of in situ salinity for altimeter heat storage estimation, *Geophys. Res. Lett.*, *27*, 549–551, 1999.

Stammer, D., C. Wunsch, and R. M. Ponte, De-aliasing of global high frequency barotropic motions in altimeter observations, *Geophys. Res. Lett.*, *27*, 1175–1178, 2000.

Tierney, C., J. Wahr, F. Bryan, and V. Zlotnicki, Short-period oceanic circulation: Implications for satellite altimetry, *Geophys. Res. Lett.*, *27*, 1255–1258, 2000.

Wang, L., C. J. Koblinsky, S. Howden, and B. Beckley, Large-scale Rossby wave in the mid-latitude South Pacific from altimetry data, *Geophys. Res. Lett.*, *25*, 179–182, 1998.

White, W. B., Annual forcing of baroclinic long waves in the tropical North Pacific Ocean, *J. Phys. Oceanogr.*, *7*, 50–61, 1977.

White, W. B., The resonant response of interannual baroclinic Rossby waves to wind forcing in the eastern midlatitude North Pacific, *J. Phys. Oceanogr.*, *15*, 404–415, 1985.

White, W. B., and J. F. T. Saur, A source of annual baroclinic waves in the eastern subtropical North Pacific, *J. Phys. Oceanogr.*, *11*, 1452–1462, 1981.

White, W. B., Y. Chao, and C.-K. Tai, Coupling of biennial oceanic Rossby waves with overlying atmosphere in the Pacific basin, *J. Phys. Oceanogr.*, *28*, 1236–1251, 1998.

Zang, X., and C. Wunch, The observed dispersion relationship for North Pacific Rossby wave motions, *J. Phys. Oceanogr.*, *29*, 2183–2190, 1999.

P. S. Polito, Divisão de Sensoriamento Remoto, Instituto Nacional de Pesquisas Espaciais, Av. dos Astronautas, 1758, São José dos Campos, São Paulo, CEP: 12227-010 Brazil. (polito@ltid.inpe.br)

W. T. Liu, Jet Propulsion Laboratory, California Institute of Technology, 4800 Oak Grove Dr., MS 300-323, Pasadena, CA 91109, USA. (liu@pacific.jpl.nasa.gov)